SCIENTIFIC REPORTS

OPEN

Observation of η-$Al_{41}Sm_5$ reveals motif-aware structural evolution in Al-Sm alloys

Received: 15 January 2018
Accepted: 2 January 2019
Published online: 30 April 2019

Z. Ye[1], F. Meng[1], F. Zhang[1], Y. Sun[1,3], L. Yang[1], S. H. Zhou[1], R. E. Napolitano[1,4], M. I. Mendelev[1], R. T. Ott[1], M. J. Kramer[1], C. Z. Wang[1] & K. M. Ho[1,2,3]

Using an effective genetic algorithm, we uncover the structure of a metastable $Al_{41}Sm_5$ phase that supplements its family sharing similar short-range orders. The phase evolves upon heating an amorphous Al-9.7 at.% Sm ribbon, produced by melt-spinning. The dynamical phase selection is discussed with respect to the structural connections between the short-range packing motifs in the amorphous precursor and those observed in the selected phases. The phase elucidated here is one of several newly discovered large-unit-cell phases found to form during devitrification from the glass in this binary system, further illustrating the power and efficiency of our approach, the important role of structural hierarchy in phase selection, and the richness of the metastable phase landscape accessible from the glassy structure.

Growing demand for advanced materials with enhanced functionality promotes expansion of the set of accessible structures. While stable materials have been efficiently identified and produced, meta-stable states are considered as a big challenge to be predicted and realized. Glass-forming alloys offer a rich landscape of non-equilibrium states, both crystalline and non-crystalline, and far-from equilibrium pathways to access them. The pathways can be manipulated through changing the starting points of materials, such as the processing parameters and the chemical composition of alloy. Al-Sm alloys, known as marginal glass formers, provide a prototypical model system where a rich collection of intermediate meta-stable crystalline phases can be accessed through path-dependent devitrification processing[1–4]. A fundamental scientific question is, what is the underlying physics mechanism of phase selections in this far-from-equilibrium system and how to control the pathways to access a myriad of meta-stable structures. A basic understanding of the physical principles that govern these pathways could very well enable application of the same principles to many different systems.

The structural orders can be a key to understanding the pathways and phase selections. Taking into account the large size and affinity disparity between Al and Sm atoms, the structural features in the Al-Sm system is most easily visualised by focusing on the the solute Sm-centered short-range order (SRO). The Al-Sm system has already exhibited a rich collection of Sm-centered ordering in known crystalline compounds, including Al_2Sm, Al_3Sm, Al_4Sm and $Al_{11}Sm_3$[1,2,5,6]. A discussion of Sm-centered SRO in these stable compounds can be found in ref.[7]. Nevertheless, the target Al-rich system (glassy structures are attainable from 7 to 13 at.% Sm) has a different composition from the above compounds, and a new Sm-cenered ordering was found in the Al-10 at.% system[7]. This Sm-centered SRO transcends liquid, glass and crystalline states. The SRO that develops in an undercooled liquid and glass plays an important role in phase selection during devitrification processes. The amorphous Al-Sm alloys realized in melt-spun ribbon and magnetron sputtered thin films devitrify following completely different pathways. Constant-heating-rate (CHR) devitrification of Al-10.2 at% Sm ribbon exhibits a polymorphic transformation that results in a cubic ε-$Al_{60}Sm_{11}$ phase[8] with a lattice parameter of ~14 Å, space group $Im\bar{3}m$ (No. 229) and with 6 unique Wyckoff positions. The thin film of the same chemical composition develops compositional inhomogeneities before the formation of fcc-Al and a hexagonal θ-Al_5Sm phase (i.e. $Al_{20}Sm_4$ in ref.[9]) with space group $P6_322$. (No. 182) and with 5 Wyckoff positions. Selection is also composition dependent, and the θ-phase is observed as the initial crystallized phase with fcc-Al during CHR devitrification of an Al-14.1% Sm melt-spun

[1]Ames Laboratory, US Department of Energy, Ames, Iowa, 50011, USA. [2]Department of Physics Iowa State University, Ames, Iowa, 50011, USA. [3]Hefei National Laboratory for Physical Sciences at the Microscale and Department of Physics, University of Science and Technology of China, Hefei, Anhui, 230026, China. [4]Department of Materials Sci. and Eng., Iowa State University, Ames, Iowa, 50011, USA. Correspondence and requests for materials should be addressed to Z.Y. (email: zye@iastate.edu) or K.M.H. (email: kmh@iastate.edu)

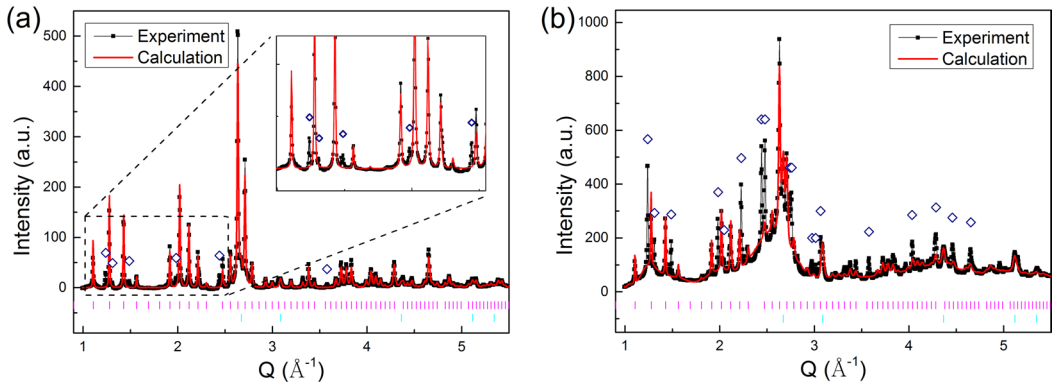

Figure 1. XRD patterns where (**a**) the unknown phase begins to appear, and (**b**) the unknown phase grows after an isothermal hold. Inset of (**a**): Amplified view of the low *Q* region, showing the peaks of the unknown phase. Black lines show the XRD pattern, while red lines show the Rietveld fitting of the XRD with ε-$Al_{60}Sm_{11}$ and fcc-Al. The vertical lines in magenta and cyan show the peak positions for ε-$Al_{60}Sm_{11}$ and Al, respectively. The navy diamonds indicate the diffraction peaks of the unknown phase.

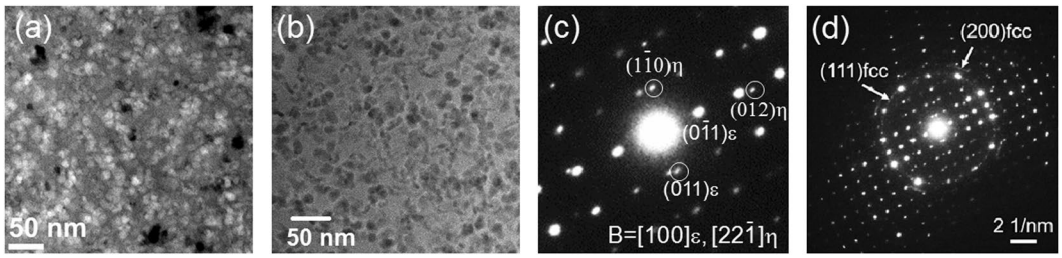

Figure 2. (**a**) Bright-field transmission electron microscopy and (**b**) high-angle annular dark-field (HAADF) scanning transmission electron microscopy images of a polyphased matrix of the metastable phases. (**c**) Zoom-in view of the corresponding selected area electron diffraction (SAD) pattern of the ε-$Al_{60}Sm_{11}$ phase and the unknown phase (designated η-$Al_{41}Sm_5$ later in this work). The zone axis is [100] for the ε-phase, and is identified later as [22$\bar{1}$] for the η-phase. (**d**) the SAD pattern that shows diffraction rings from nanocrystalline fcc-Al grains.

ribbon. The ε-$Al_{60}Sm_{11}$ and θ-Al_5Sm phases share the same Sm-centered first-shell atomic packing "3-6-6-1" motif[7,8] (referred to as "T6" in ref.[7]). The same 3-6-6-1 motif is found dominant in undercooled liquids, indicating a clear structural inheritance from the liquid to its devitrified crystalline phases.

We have recently developed an approach to solve for undetermined complex crystal structures observed in far-from equilibrium transitions[8,9]. The approach integrates lattice and space group information from X-ray diffraction (XRD) analysis with a genetic algorithm (GA) structural search. With this approach, we have successfully identified several previously unknown large unit-cell (LUC) structures, including the ε-$Al_{60}Sm_{11}$ phase[8] and the θ-Al_5Sm phase (i.e. $Al_{20}Sm_4$ in ref.[9]). Presently, we report on the discovery and identification of a LUC (~90 atoms/cell) tetragonal structure, termed hereafter as η-$Al_{41}Sm_5$ in this work.

The unknown phase appears as a part of a polyphase assembly of metastable phases that evolve during devitrification of an amorphous Al-9.7% Sm melt spun ribbon. The existence of common Sm-centered first-shell packing motifs in each of these LUC crystal structures (ε, θ, and η phases) provides clear evidence for the critical role of structural hierarchy in complex phase selection in Al-Sm alloys. The structural hierarchy is referred to as the similarity of Sm-centered short-range order between a phase and its successor phase along the devitrification pathway starting from glass. In this picture, specific short-range packing motifs which contribute to glassy behavior in undercooled liquids and amorphous solids also serve as precursors for particular crystalline phases that appear during initial stages of devitrification.

Results

Experimental characterization. Upon CHR heating, the amorphous ribbon exhibits a multi-step devitrification pathway that is characterized by a series of metastable crystalline phases[2,10]. The first devitrified phases are the ε-$Al_{60}Sm_{11}$, fcc-Al and a small fraction of an unknown phase, as indicated by several minor XRD peaks marked by diamonds that cannot be indexed in Fig. 1(a). With an isothermal hold at 464 K, the unknown phase grows as indicated in the enhanced peaks in XRD as shown in Fig. 1(b). More peaks of the unknown phase are also observed to appear in Fig. 1(b). Figure 2(a–d) show the bright field transmission electron microscopy (BF-TEM) image, high angle annular dark field scanning transmission electron microscopy (HAADF-STEM) image and selected area diffraction (SAD) pattern, respectively. Figure 2(c) is a zoom-in view of SAD pattern

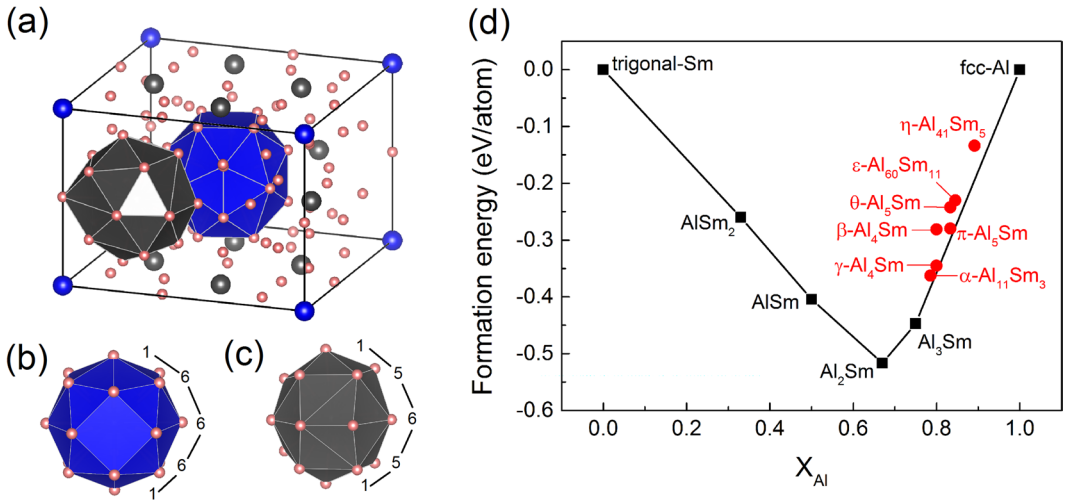

Figure 3. (**a**) The structure of η-$Al_{41}Sm_5$ showing two Sm-centered motifs: (**b**) the 1-6-6-6-1 motif marked in blue, and (**c**) the 1-5-6-5-1 motif in grey. Pink (blue/grey) represents Al (Sm) atoms. (**d**) The formation energy of known stable and meta-stable phases at 0 K as a function of the Al composition. The solid line connects the thermodynamically stable phases (black squares) shown in the phase diagram. The red circles are the meta-stable phases.

in Fig. 2(d), which shows the diffraction patterns of the ε-phase and the unknown η-phase. Diffraction rings from nanocrystalline fcc-Al grains are shown in Fig. 2(d). Figure 2(c,d) suggest the grain size of the ε- and the η-phases are much larger than fcc-Al particles. However, as Fig. 2(a,b) indicate, the grain boundaries between ε/ε, ε/η, and η/η are not clearly observed, probably due to the high density of fcc-Al particles dispersed (see also Supplementary Fig. S1).

Identification of the unknown phase. The complex structure of the unknown phase was determined by employing the approach described in ref.[8]. Using standard space group peak-matching techniques to analyze the XRD pattern shown in Fig. 1(b), we initially identify the unit cell as body-centered tetragonal with lattice parameters, a = 13.33 Å and c = 9.59 Å. Based on an assumed density equal to that of the glass (0.051 atoms/Å^3), we estimate the number of atoms per unit cell to be approximately 90. Using a classical interatomic potential for computational expediency[11], we perform a GA search, seeking low-energy structures with the tetragonal unit cell and the space group of $I4$ and $I\bar{4}$. The search is followed by computing an XRD pattern for each structure in the GA pool using the Rietveld program RIETAN-FP[12] and first-principles density function theory (DFT) energy calculations[13–17]. A profile factor F_{XRD} is calculated to assess how well the computed pattern fits the experiment measurements[8,9]. A lower F_{XRD} indicates a better match with the experimental XRD pattern. After selecting a small set of candidate structures based on the F_{XRD}, a more accurate DFT energy is calculated[13] for each structure.

There are a series of crystal structures in the GA pool with both low F_{XRD} and low energy. Among them, the structure exhibiting the lowest formation energy is shown in Fig. 3(a). More details about other structures can be found in the discussion. The phase, designated here as η, exhibits a tetragonal unit cell with space group No. 87 (I4/m) including 10 Wyckoff positions and a stoichiometry of $Al_{82}Sm_{10}$. With two formula units per unit cell, the complete designation for this phase becomes η-$Al_{41}Sm_5$. The formation energy is 0.051 eV/atom with respect to fcc-Al and Al_3Sm. It also has a low F_{XRD}, which indicates a good match with experiment XRD, as shown in Fig. 4. Figure 3(d) shows the formation energy with respect to trigonal-Sm and fcc-Al of known stable, metastable phases, and the recently solved metastable phases π-Al_5Sm[4], ε-$Al_{60}Sm_{11}$[8], θ-Al_5Sm[9], and η-$Al_{41}Sm_5$. To distinguish the 2*b* and 8*h* Sm sites, they are marked in Fig. 3(a) with blue and grey, respectively. We highlight here the first shell packing environments around the 2 Sm sites, as illustrated with blue and grey polyhedral. The motif around the 2*b* and 8*h* Sm site is termed as 1-6-6-6-1 and 1-5-6-5-1, respectively, based on the packing of the atoms around the Sm atom as shown in Fig. 3(b,c).

Rietveld refinement. A Rietveld fitting is done to refine the lattice and atomic positions. We choose to fit the data at 464 K, and the result in Fig. 4 reveals three different phases: the cubic ε-$Al_{60}Sm_{11}$, fcc-Al and the tetragonal η-$Al_{41}Sm_5$, which constitute ~33.3, 38.3, and 28.4 wt.%, respectively. Table 1 shows the lattice parameters and atomic coordinates of the η-$Al_{41}Sm_5$ phase, given by both DFT calculations and the Rietveld analysis.

Free energy calculation. At 0 K, the η-$Al_{41}Sm_5$ phase is 0.051 eV/atom unstable with respect to phase separation into the Al_3Sm phase and pure Al. To investigate the effects of finite temperatures, we calculated the Gibbs free energy energy within the quasi-harmonic approximation using the Phonopy package[18]. At a fixed volume, the Holmoltz free energy under the harmonic approximation is given by

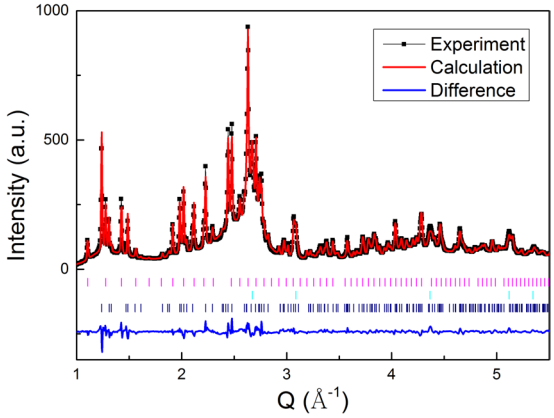

Figure 4. Rietveld fitting of the XRD patterns for melt spun Al-9.7% Sm ribbon at 464 K, showing the crystallization products of the cubic ε-$Al_{60}Sm_{11}$, fcc-Al and the tetragonal η-$Al_{41}Sm_5$. The vertical lines in magenta, cyan, and navy show the diffraction peak positions for ε-$Al_{60}Sm_{11}$, Al and η-$Al_{41}Sm_5$, respectively. The fitting of the experimental data gives wRp = 0.0577 and Rp = 0.0398, where wRp and Rp are the weighted and unweighted profile R-factors, respectively[26].

Lattice parameters (in unit of Å)				
a = 13.284 (13.347), c = 9.568 (9.590)				
Atomic coordinates				
	X	Y	Z	Wyckoff
Al1	0.619 (0.610)	0.282 (0.287)	0	8 h
Al2	0.097 (0.095)	0.522 (0.516)	0	8 h
Al3	0.136 (0.138)	0.074 (0.069)	0.191(0.179)	16i
Al4	0.572 (0.568)	0.136 (0.146)	0.252 (0.244)	16i
Al5	0.564 (0.571)	0.725 (0.720)	0.145 (0.148)	16i
Al6	0.25	0.25	0.25	8 f
Al7	0	0	0	2a
Al8	0.840 (0.847)	0.282 (0.280)	0	8 h
Sm1	0.927 (0.926)	0.722 (0.723)	0	8 h
Sm2	0	0	0.5	2b

Table 1. Lattice parameters and atomic coordinates of the η-$Al_{41}Sm_5$ phase with the space group No. 87 (I4/m). The numbers in parentheses are given by Rietveld analysis, and the rest by DFT calculations.

$$F = E_0 + k_B T \sum_{nk} \ln\left[2 \sinh \frac{\hbar\omega_n(k)}{2k_B T}\right], \tag{1}$$

where E_0 is the zero-temperature total energy from VASP calculation, and $\omega_n(k)$ is the phonon spectrum. To account for thermal expansion, the phonon spectrum is calculated at various volumes, and the Gibbs free energy G is obtained by minimizing F with respect to the volume[18]. In Fig. 5(a), we first show the phonon density of states of the η-$Al_{41}Sm_5$ phase at 0 K. No negative phonon modes were observed, indicating that the η-$Al_{41}Sm_5$ phase is mechanically stable. In Fig. 5(b), we plot the formation Gibbs free energy, referenced to fcc-Al and Al_3Sm, as a function of temperature, where one can see that the η-$Al_{41}Sm_5$ phase remains unstable w.r.t. Al and Al_3Sm ($G_{form} > 0$) for the entire temperature range of the devitrification process. However, G_{form} decreases with the temperature, showing that it becomes more stable as temperature increases. It should be noted that our calculation did not fully address the aharmonicity in the system, which can have non-negligible effects at higher temperatures. Approaches that can deal with such effects, such as the thermodynamic-integration method[19], are much more demanding computationally, and are rarely applied at the ab-initio level. Meanwhile, we believe that more accurate calculations will not change the marginally unstable nature of the η-phase.

Discussion

A series of similar crystal structures are found in the GA search with low F_{XRD} and low energy. Figure 6 shows the first 3 crystal structures with the lowest formation energy. The 3 structures have a tetragonal unit cell with slightly different stoichiometries. The distribution of Sm atoms are very similar but a varience in the distribution of Al atoms is observed probabaly because the number of Al atoms are different. All the 3 structures have the 1-6-6-6-1

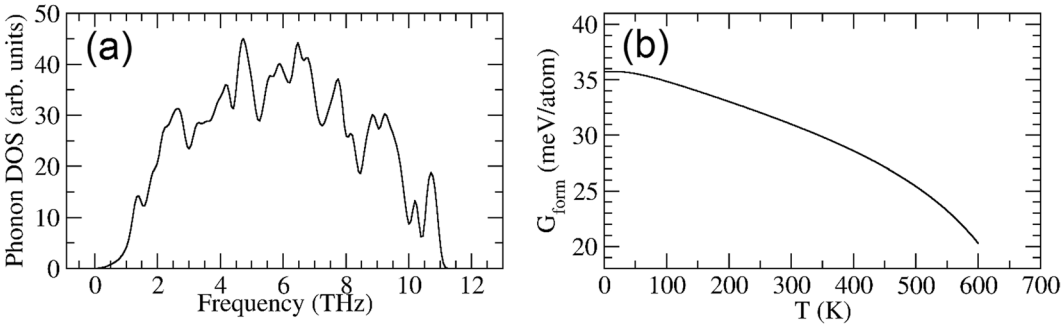

Figure 5. (**a**) Phonon density of states of the η-$Al_{41}Sm_5$ phase. (**b**) The formation Gibbs free energy as a function of the temperature referenced to Al and Al_3Sm.

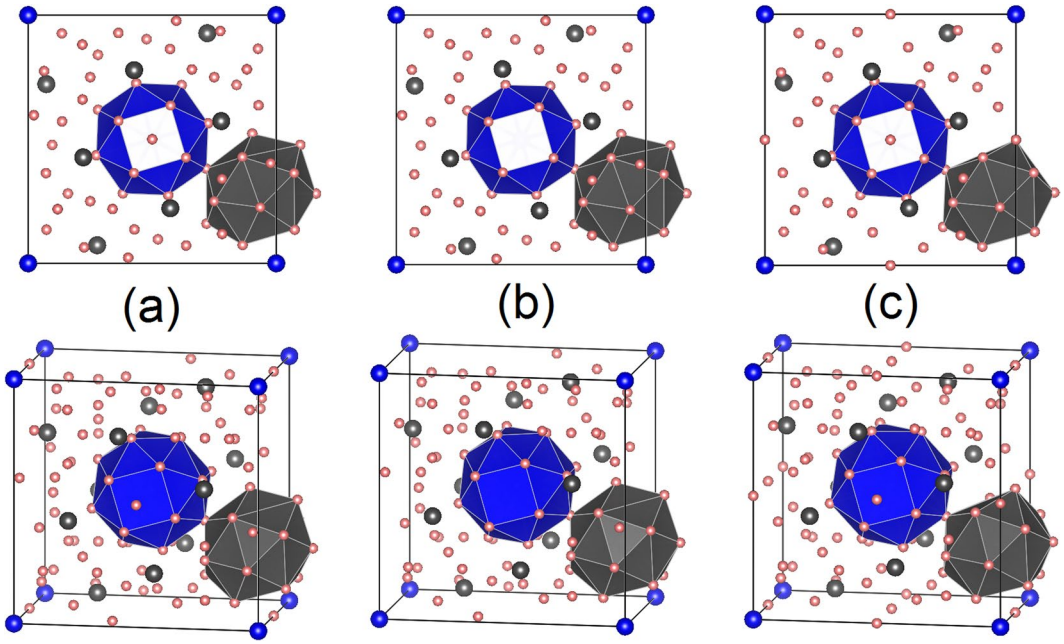

Figure 6. The crystal structures with lowest formation energy: (**a**) $Al_{82}Sm_{10}$ (e.g. the η-$Al_{41}Sm_5$ phase), (**b**) $Al_{80}Sm_{10}$, and (**c**) $Al_{78}Sm_{10}$ with formation energy of 0.051, 0.055, and 0.063 eV/atom respectively, w.r.t. fcc-Al and Al_3Sm. All 3 structures have the 1-6-6-6-1 motif marked in blue. Pink (blue/grey) represents Al (Sm) atoms.

motif. The other motif marked in grey is somewhat different in $Al_{78}Sm_{10}$. We note that it is usually hard to determine the exact structure of a complicated crystal with a big unit cell like this. Instead a series of similar structures can be found, all of which are characterized by a common Sm-centered 1-6-6-6-1 motif. The one with the lowest formation energy, $Al_{82}Sm_{10}$ (e.g. the η-$Al_{41}Sm_5$ phase), is picked up for Rietveld refinement and free energy calculation.

While lacking long-range translational symmetry, the as-quenched Al-Sm glasses, like many glasses, have clear elements of short range order (SRO). In particular, these Sm-centered packing motifs, play a crucial role in phase selection during devitrification. In simulated undercooled Al-10% Sm liquids, the "3-6-6-1" motif is the dominant Sm-centered motif[7]. Experimentally the Al-Sm glasses can be synthesized by melt spinning and magnetron sputtering. As shown in Fig. 7, the θ-Al_5Sm phase (along with fcc-Al) precipitates from the amorphous sputtered Al-10% Sm thin film[9]. The θ-Al_5Sm structure is composed exclusively of the same "3-6-6-1" motif, indicating a well-defined structural order that transcends glass and its devitrified crystalline phase. The ε-$Al_{60}Sm_{11}$ phase[8] precipitates from the amorphous melt spun Al-10.2% Sm ribbon. The ε-$Al_{60}Sm_{11}$ phase also exhibits the same "3-6-6-1" motif, indicating a clear structural inheritance from the glass. In addition, it has another "1-6-6-6-1" motif[8]. The η-$Al_{41}Sm_5$ phase appears with a small fraction along with the ε-$Al_{60}Sm_{11}$ phase devitrified from the melt spun Al-9.7% Sm ribbon. It grows with an enhanced fraction under an isothermal hold. The η-$Al_{41}Sm_5$ phase is composed of the same "1-6-6-6-1" as in the ε-$Al_{60}Sm_{11}$ phase and a new "1-5-6-5-1" motif as shown in Fig. 3(a–c). The appearance of similar cluster motifs between the ε-$Al_{60}Sm_{11}$ and the η-$Al_{41}Sm_5$ phases provides another solid evidence for the structural hierarchy mechanism of complex phase selections in Al-Sm alloys. The question remains, however, as to whether the η-$Al_{41}Sm_5$ phase is formed directly from the glass

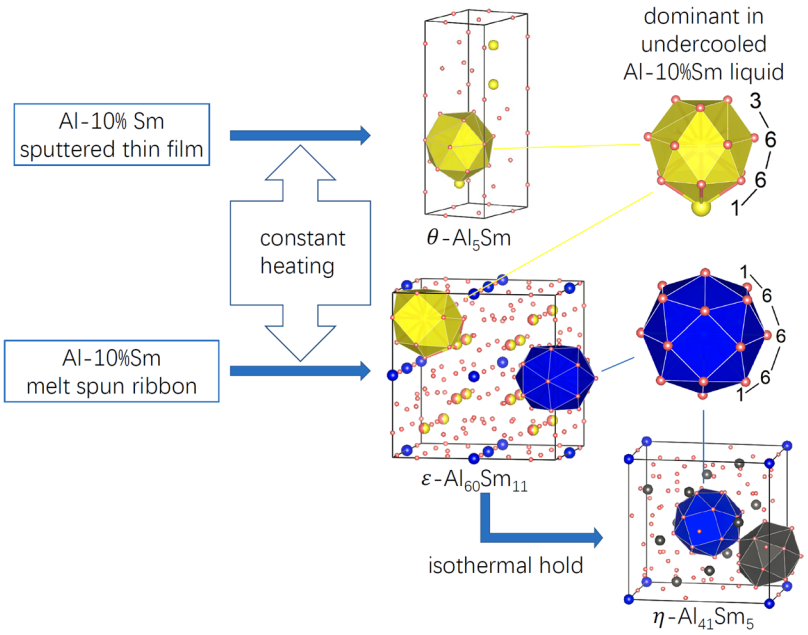

Figure 7. The structural hierarchy in the devitrification pathways of Al-10at.% Sm magnetron sputtered thin film and melt spun ribbon. The θ- and ε-phases share the same 3-6-6-1 motif as dominant in undercooled liquid. The η- and ε-phases share another 1-6-6-6-1 motif.

or the ε-$Al_{60}Sm_{11}$ phase is a precursor for the formation of the η-$Al_{41}Sm_5$ phase. It is open to question as well why the sputtered or the melt-spun material would prefer the formation of a particular phase instead of others. The medium-range order (MRO), or how the local motifs are packed at medium range, may also strongly affect the complex phase selection. Different MROs are observed with different processing methods or thermal treatments. A laser pretreatment changes MRO in Ag/In-incorporated Sb_2Te[20]. Magnetron-sputtered and pure ion-implanted amorphous silicon exhibit significantly different SRO and MRO following thermal annealing[21]. Different distribution of icosahedral- and crystal-like superclusters are observed with varying annealing temperature in simulated $Zr_{50}Cu_{45}Al_5$ bulk metallic glass[22]. While these studies have advanced our comprehension of structural order in amorphous materials, detailed discussion of MRO is beyond the scope of this work.

In summary, we observed an unknown metastable phase during the devitrification of melt spun Al-10% Sm glasses. Using an efficient genetic algorithm combined with experimental diffraction data, we found a series of similar crystal structures which have low energy and fit well with the experiment XRD. The crystalline phase with the lowest formation energy, termed η-$Al_{41}Sm_5$, has a big tetragonal unit cell that contains 92 atoms with the stoichiometry $Al_{82}Sm_{10}$. The calculated X-ray diffraction pattern matches well with that of the experiments. η-$Al_{41}Sm_5$ is mechanically stable from phonon spectrum calculation. It is metastable with respect to phase separation into Al_3Sm and pure Al at finite temperatures. Resolution of the atomic structure of these new metastable complex crystal phases lay the groundwork for further investigations to elucidate how different processing protocols can influence the selection and growth of different metastable crystal phases in the devitrification process. Examining the 3 metastable phases observed so far in devitrification experiments, we find a common picture emerging where complex metastable phases which appear have structures dominated by specific atomic clusters (motifs) centered about Sm atoms. This supports structure hierarchy picture of complex phase formations and suggests a possible physical mechanism where the low mobility of Sm atoms during devitrification process plays an important role in the selection of metastable crystal phases compatible with certain Sm-centered cluster motifs.

Methods

Preparation of the amorphous alloy. Alloys of Al-9.7% Sm were prepared in ingots of 10 grams by simultaneously arc-melting the pure components (99.99 wt% Al and 99.9 wt% Sm) under an Ar atmosphere. The alloy ingots were re-melted under 1/3 atm argon and rapidly solidified into ribbons (0.02–0.03 mm thick) by free-jet melt-spinning onto a rotating Cu wheel (tangential speed of 30 m/s). Both high resolution transmission electron microscopy (TEM) and high energy X-ray diffraction (HEXRD) reveal the amorphous nature without any detectable crystallized phase (not shown here).

Crystallization of the amorphous alloy. Crystallization of the amorphous alloy ribbons was investigated using time-resolved synchrotron-based HEXRD (71.77 keV energy, 0.1729 Å wavelength), utilizing the 1-ID-E beamline of the Advanced Photon Source (APS) at Argonne National Laboratory. Specimens for HEXRD were prepared by cutting melt-spun ribbon into lengths of approximately 10 mm, stacking multiple segments to a thickness of ~0.5 mm, and inserting into a 2 mm ID thin walled SiO_2 capillary tube which was sealed under argon. An infrared heater was used for *in-situ* heating and isothermal holding. HEXRD pattern revealed that the

ε-$Al_{60}Sm_{11}$ phase and a small amount of fcc-Al were the first phases to appear during devitrification. There were several minor XRD peaks that cannot be indexed, as marked by diamonds in Fig. 1(a), suggesting a small fraction of an unknown phase mixed with the ε-$Al_{60}Sm_{11}$ phase and fcc-Al. With an isothermal hold at 464 K (about 5 K lower than the onset temperature for crystallization) for 70 mins, the unknown phase grew as indicated in the enhanced peaks in XRD as shown in Fig. 1(b). Post-devitrification samples were analyzed using TEM (Tecnai G^2 F20). TEM specimens were prepared using a dual-beam focused ion beam (FIB) instrument (FEI Helios NanoLab G3 UC). BF-TEM, HAADF-STEM images and SAD pattern (Fig. 2(a–d)) were obtained to analyze the post-devitrification samples. The BF-TEM image shown in Fig. 2(a) and the HAADF-STEM image in Fig. 2(b) clearly demonstrated a fully crystallized polyphase material. The nanocrystals uniformly distributed in the matrix with grain size of ~20–30 *nm* in Fig. 2(a) were fcc-Al, which corresponded to the dark region (low *z*-contrast) in HAADF-STEM image of Fig. 2(b).

Genetic algorithm (GA). A GA was used to search for low energy structures by defining the fitness as a function of energy. All structure relaxations during the GA search were performed by LAMMPS code[23] with Embedded-Atom Method (EAM) potential in Finnis-Sinclair form[24]. As previously shown[4,11], this FS potential fitted to first principles calculation data, in general, gives a satisfactory estimation of the relative thermodynamic stability of the known stable and meta-stable phases.

Density Functional Theory (DFT). After a GA search for low energy structures using EAM potential, a more accurate DFT energy was calculated for a selection of structures which are a good match with experiment XRD. All DFT calculations were performed using the Vienna *ab initio* simulation package (VASP)[14] with the projector-augmented wave (PAW) pseudopotential method[15,16] and the generalized-gradient approximation (GGA)[17].

Fitting XRD pattern. A standard Rietveld analysis was carried out using the GSAS package and the EXPGUI interface[25] to refine the η-$Al_{41}Sm_5$ structure from GA search and DFT calculation. Lattice parameter, atomic coordinates, site occupancies, thermal parameters, and peak shape profiles are refined to get the XRD pattern in Fig. 4. Lattice parameters and atomic coordinates given by DFT calculations and the Rietveld analysis are provided in Table 1.

References

1. Guo, J. Q., Ohtera, K., Kita, K., Nagahora, J. & Kazama, N. S. Crystallization behavior of $Al_{100-x}Sm_x$ (x = 8–14 at%) amorphous alloys. *Mater. Lett.* **24**, 133–138 (1995).
2. Rizzi, P., Baricco, M., Borace, S. & Battezzati, L. Phase selection in Al-TM-RE alloys: Nanocrystalline Al versus intermetallics. *Mater. Sci. Eng. A* **304–306**, 574–578 (2001).
3. Kalay, Y. E., Yeager, C., Chumbley, L. S., Kramer, M. J. & Anderson, I. E. Initial crystallization in a nanostructured Al-Sm rare earth alloy. *J. Non. Cryst. Solids* **356**, 1416–1424 (2010).
4. Zhang, F. *et al*. Discovery of a meta-stable Al-Sm phase with unknown stoichiometry using a genetic algorithm. *Scr. Mater.* **81**, 32–35 (2014).
5. Battezzati, L., Baricco, M., Schumacher, P., Shih, W. C. & Greer, A. L. Crystallization behaviour of Al-Sm amorphous alloys. *Mater. Sci. Eng.* **179**, 600–604 (1994).
6. Okamoto, H. A.-S. *J. Phase Equilib. Diffus.* **33**, 243, https://doi.org/10.1007/s11669-012-0019-y (2012).
7. Sun, Y. *et al*. Crystal Genes' in Metallic Liquids and Glasses. *Sci. Rep.* **6**, 23734 (2016).
8. Ye, Z. *et al*. Structural hierarchy as a key to complex phase selection in Al-Sm. *Phys. Rev. Materials* **1**, 055601 (2017).
9. Ye, Z. *et al*. Discovery of a metastable $Al_{20}Sm_4$ phase. *Appl. Phys. Lett.* **106**, 101903 (2015).
10. Kalay, Y. E., Chumbley, L. S. & Anderson, I. E. Crystallization behavior in a highly driven marginal glass forming alloy. *J. Non. Cryst. Solids* **354**, 3040–3048 (2008).
11. Mendelev, M. I. *et al*. Development of interatomic potentials appropriate for simulation of devitrification of $Al_{90}Sm_{10}$ alloy. *Model. Simul. Mater. Sci. Eng.* **23**, 045013 (2015).
12. Izumi, F. & Momma, K. Three-Dimensional Visualization in Powder Diffraction. *Solid State Phenom.* **130**, 15–20 (2007).
13. Kohn, W. & Sham, L. J. Self-consistent equations including exchange and correlation effects. *Phys. Rev.* **140**, A1133 (1965).
14. Kresse, G. & Furthmuller, J. Efficiency of ab-initio total energy calculations for metals and semiconductors using a plane-wave basis set. *Comput. Mater. Sci.* **6**, 15–50 (1996).
15. Blochl, P. E. Projector augmented-wave method. *Phys. Rev. B* **50**, 17953 (1994).
16. Kresse, G. & Joubert, D. From ultrasoft pseudopotentials to the projector augmented-wave method. *Phys. Rev. B* **59**, 1758 (1999).
17. Perdew, J. P., Burke, K. & Ernzerhof, M. Generalized Gradient Approximation Made Simple. *Phys. Rev. Lett.* **77**, 3865–3868 (1996).
18. Togo, A. & Tanaka, I. First principles phonon calculations in materials science. *Scr. Mater.* **108**, 1–5 (2015).
19. Frenkel, D. & Smit, B. *Understanding Molecular Simulation: From Algorithms to Application*. (Academic Press, 2007).
20. Lee, B. S. *et al*. Observation of the Role of Subcritical Nuclei in Crystallization of a Glassy Solid. *Science* **326**, 980–984 (2009).
21. Haberl, B. *et al*. Unexpected short- and medium-range atomic structure of sputtered amorphous silicon upon thermal annealing. *J. Appl. Phys.* **110**, 096104 (2011).
22. Hwang, J. *et al*. Nanoscale Structure and Structural Relaxation in $Zr_{50}Cu_{45}Al_5$ Bulk Metallic Glass. *Phys. Rev. Lett.* **108**, 195505 (2012).
23. Plimpton, S. Fast Parallel Algorithms for Short-range Molecular Dynamics. *J. Comput. Phys.* **117**, 1–19 (1995).
24. Finnis, M. W. & Sinclair, J. E. A Simple Empirical N-Body Potential for Transition Metals. *Phil. Mag. A* **50**, 45–55 (1984).
25. Toby, B. H. EXPGUI, a Graphical User Interface for GSAS. *J. Appl. Cryst.* **34**, 210–213 (2001).
26. The Rietveld software package GSAS is used to fit the experiment XRD pattern. The definition of wRp and Rp can be found in the GSAS manual, https://subversion.xray.aps.anl.gov/EXPGUI/gsas/all/GSAS%20Manual.pdf.

Acknowledgements

Work at Ames Laboratory was supported by the US Department of Energy, Basic Energy Sciences, Materials Science Division and Engineering, under Contract No. DE-AC02-07CH11358, including a grant of computer time at the National Energy Research Supercomputing Center (NERSC) in Berkeley, CA. The high-energy X-ray experiments were performed at the XOR beamline (sector 1) of the Advanced Photon Source, Argonne National Laboratory, under Grant No. DE-AC02-06CH11357.

Author Contributions

K.M.H. and C.Z.W. designed and supervised the project. Z.Y., F.Z., Y.S. and L.Y. performed GA search. F.M., R.T.O., M.J.K., S.Z. and R.E.N. designed and performed experiments and XRD measurements. M.I.M. developed the Finnis-Sinclair potential for the Al-Sm system. Z.Y. and M.J.K. performed the Rietveld refinement. F.Z. performed free energy calculation. Z.Y., F.M., and F.Z. wrote the paper.

Additional Information

Supplementary information accompanies this paper at https://doi.org/10.1038/s41598-019-43079-9.

Competing Interests: The authors declare no competing interests.

Publisher's note: Springer Nature remains neutral with regard to jurisdictional claims in published maps and institutional affiliations.